

REPORT DOCUMENTATION PAGE

AFRL-SR-AR-TR-05-

0488

Public reporting burden for this collection of information is estimated to average 1 hour per response, including the time for reviewing the data needed, and completing and reviewing this collection of information. Send comments regarding this burden estimate or an reducing this burden to Washington Headquarters Services, Directorate for Information Operations and Reports, 1215 Jefferson Da Management and Budget, Paperwork Reduction Project (0704-0188), Washington, DC 20503

1. AGENCY USE ONLY (Leave blank)		2. REPORT DATE 22-Aug-05	3. REPORT TYPE AND DATES COVERED 15June02 to 14March05 Final	
4. TITLE AND SUBTITLE Imaging and Inversion Using Sparse Arrays			5. FUNDING NUMBERS Grant # F49620-02-1-0309	
6. AUTHOR(S) Dr Anthony Devaney				
7. PERFORMING ORGANIZATION NAME(S) AND ADDRESS(ES) A.J. Devaney Associates, Inc 12 Orchard Hill Harvard, MA 01451			8. PERFORMING ORGANIZATION REPORT NUMBER 0002AA Final	
9. SPONSORING / MONITORING AGENCY NAME(S) AND ADDRESS(ES) Air Force Office of Scientific Research 875 No. Randolph St Rm 3112 Arlington, VA 22203 NM			10. SPONSORING / MONITORING AGENCY REPORT NUMBER 0002 AA	
11. SUPPLEMENTARY NOTES				
12a. DISTRIBUTION / AVAILABILITY STATEMENT Approved for public release distribution unlimited			12b. DISTRIBUTION CODE	
13. ABSTRACT (Maximum 200 Words) The inverse scattering problem is solved within the distorted wave Born approximation (DWBA) using a generalized time reversal based formulation. The theory is applicable to arbitrary (non-point) N~ element transmitter arrays and N0 element receiver arrays and to scattering systems chara tensed by scattering potentials interrogated in a set of scattering experiments employing single or multiple temporal frequencies. The inversion scheme generates a pseudo-inverse reconstruction of the scattering potential based on the SVD of the N0 x N0 multistatic data matrix considered as a mapping from the llibert space of scattering potentials to the vector space of N0 x N0 >< N~ complex N-tuples, where N~ is equal to the number of discrete temporal frequencies employed in the set of scattering experiments. The theory and results in this report have been previously published and appear in: 1. A.J. Devaney and M. Dennison, "Inverse Scattering In Inhomogeneous Background Media," Inverse Problems 19, No. 4 (August 2003), 855-870, 2. M. Demsison and A.J. Devaney, "Inverse scattering in inhomogeneous background media;Part II SVD analysis and multiple frequency case, Inverse Problems, 20, 2004, 1307-1324.				
14. SUBJECT TERMS inversion and imaging using sparse arrays			15. NUMBER OF PAGES 18	
			16. PRICE CODE- grant	
17. SECURITY CLASSIFICATION OF REPORT unclassified	18. SECURITY CLASSIFICATION OF THIS PAGE unclassified	19. SECURITY CLASSIFICATION OF ABSTRACT unclassified	20. LIMITATION OF ABSTRACT SAR	

NSN 7540-01-280-5500

Standard Form 298 (Rev. 2-89)
Prescribed by ANSI Std. Z39-18
298-102

Inverse Scattering in Inhomogeneous Background Media

FINAL REPORT

Contract # F49620-02-1-0309

A.J. Devaney
A.J. Devaney Associates, Inc.

Abstract

The inverse scattering problem is solved within the distorted wave Born approximation (DWBA) using a generalized time reversal based formulation. The theory is applicable to arbitrary (non-point) N_α element transmitter arrays and N_β element receiver arrays and to scattering systems characterized by scattering potentials interrogated in a set of scattering experiments employing single or multiple temporal frequencies. The inversion scheme generates a pseudo-inverse reconstruction of the scattering potential based on the SVD of the $N_\beta \times N_\alpha$ multistatic data matrix considered as a mapping from the Hilbert space of scattering potentials to the vector space of $N_\beta \times N_\alpha \times N_\omega$ complex N-tuples, where N_ω is equal to the number of discrete temporal frequencies employed in the set of scattering experiments. The theory and results in this report have been previously published and appear in: 1. A.J. Devaney and M. Dennison, "Inverse Scattering In Inhomogeneous Background Media," *Inverse Problems* **19**, No. 4 (August 2003), 855-870, 2. M. Dennison and A.J. Devaney, "Inverse scattering in inhomogeneous background media: Part II SVD analysis and multiple frequency case," *Inverse Problems*, **20**, 2004, 1307-1324.

1 Introduction

The research reported herein was conducted over the past three years and consisted of the extension of the methods of time reversal based *imaging* to applications of *inverse scattering*. The foundations of the developed theory were published in 2003 in [1] and applied to the inverse scattering problem for frequency dependent, compactly supported scattering potentials formulated within the distorted wave Born approximation (DWBA) [2]. In that paper the scattering object was assumed to be embedded in a known background medium and the distorted wave Born approximation to the Lippmann Schwinger equation was shown to lead to a simple expression for the so-called *multistatic data matrix* $K(\beta_j, \alpha_k, \omega)$. This latter quantity is the scattered field amplitude at receiver point β_j due to point source excitation at transmitter point α_k and temporal frequency ω and was assumed to be known (measured) over some arbitrary set of transmitter and receiver points indexed by $k = 1, 2, \dots, N_\alpha$, $j = 1, 2, \dots, N_\beta$ and at some fixed frequency ω . A Hilbert space formulation of the inverse scattering problem thus stated was then employed that lead in a simple way to an inversion algorithm that generates a least squares, pseudo-inverse of the scattering potential at the given temporal frequency ω .

The theory and results established in [1] were extended in [3] to be applicable to non-point transmitter and receiver elements and to dispersionless scattering potentials for which the scattering data are known at multiple temporal frequencies ω_f , $f = 1, 2, \dots, N_\omega$. Although both generalizations were found to be simple extensions of the underlying theory presented in the earlier paper and require only minor changes in notation and implementation they can be important in practical applications that generally employ extended 2D antenna or transducer elements and broadband or stepped frequency excitation.

The least squares, pseudo-inverse inversion schemes developed in the grant are based on the singular value decomposition (SVD) of the underlying DWBA mapping $\mathcal{P} : H_V \rightarrow C^N$, where H_V is the Hilbert space of compactly supported scattering potentials and C^N the space of complex N tuples where $N = N_\beta \times N_\alpha \times N_\omega$. I emphasize that the use of the SVD employed here to solve the inverse scattering problem is vastly different from its conventional use in other time-reversal based imaging and inverse scattering applications [4, 5, 6] where it is used to decompose the linear mapping from the incident field to the scattered field. In the study reported here, it is used to decompose the mapping from the Hilbert space of compactly supported scattering potentials to the finite-dimensional vector space representing the scattered field data. These two mappings, and associated SVD's, are totally different and are directly applicable to different classes of problems.

DISTRIBUTION STATEMENT A
Approved for Public Release
Distribution Unlimited

20051214 029

2 Problem Formulation and Review of [1]

I consider the general scenario of a scattering object compactly supported in some volume \mathcal{V} that is embedded in a known inhomogeneous background medium and is interrogated in a set of N_α scattering experiments where in each experiment the incident wave is generated by a point source located at α_k , $k = 1, 2, \dots, N_\alpha$ and the scattered wave is measured over a set of N_β point receiving sensors located at β_j , $j = 1, 2, \dots, N_\beta$. The suite of data obtained from these experiments is called the *multistatic data matrix* and, within the so-called *distorted wave Born approximation* (DWBA)[2], is related to the object's scattering potential via the equation [1]

$$K_{j,k}(\omega) = \int_{\mathcal{V}} d^3r G_0(\beta_j, \mathbf{r}, \omega) O(\mathbf{r}, \omega) G_0(\mathbf{r}, \alpha_k, \omega), \quad (1)$$

where ω is the temporal frequency, $O(\mathbf{r}, \omega)$ is the object's (generally complex) scattering potential relative to the known background and G_0 is the background Green function which is assumed known. The multistatic data matrix $K_{j,k}$ can be directly measured at one or more frequencies ω via monochromatic source excitation or, alternatively, can be computed over a large set of frequencies via Fourier transformation of the measured responses from pulse excitation.

By defining

$$D_n(\omega) = K_{j,k}(\omega), \quad n = j + (k-1)N_\beta, \quad j = 1, 2, \dots, N_\beta, \quad k = 1, 2, \dots, N_\alpha, \quad (2)$$

we can regard the relationship Eq.(1) to be a linear mapping from the Hilbert space $H_{\mathcal{V}}$ of complex valued scattering potentials $O(\mathbf{r}, \omega)$ compactly supported in \mathcal{V} to the finite dimensional vector space $C^N(\omega)$ of complex N-tuples $D = \{D_n(\omega)\}$, $n = 1, 2, \dots, N$ where $N = N_\beta \times N_\alpha$. Following the treatment presented in [1] I express Eq.(1) in the form

$$\mathcal{P}O(\omega) = D(\omega) \quad (3)$$

where \mathcal{P} is the integral operator $H_{\mathcal{V}} \rightarrow C^N(\omega)$:

$$\mathcal{P} = \int_{\mathcal{V}} d^3r \pi_n^*(\mathbf{r}, \omega), \quad (4a)$$

with

$$\pi_n(\mathbf{r}, \omega) = \begin{cases} G_0^*(\beta_j, \mathbf{r}, \omega) G_0^*(\alpha_k, \mathbf{r}, \omega) & \text{if } \mathbf{r} \in \mathcal{V} \\ 0 & \text{else-wise.} \end{cases} \quad (4b)$$

The above set of equations provide the underlying formulation of the inversion scheme developed in the grant and reported in [1] and in [3].

2.1 Pseudo-inverse of the DWBA mapping

At each frequency ω the distorted wave Born approximation (DWBA) mapping Eq.(3) defines a projection of the unknown scattering potential $O(\mathbf{r}, \omega)$ onto the subspace $H_{\mathcal{V}} = \text{Span}\{\pi_n\} \subset H_{\Pi}$ of $H_{\mathcal{V}}$ that is spanned by the set of functions $\{\pi_n(\mathbf{r}, \omega)\}$, $n = 1, 2, \dots, N$. This fact was the basis for the pseudo-inverse of this mapping presented in [1] where the pseudo-inverse $\hat{O}(\mathbf{r}, \omega)$ was expanded into the set of spanning functions π_n with coefficients C_n that were computed by direct matrix inversion. Thus, in particular, we have that

$$\hat{O}(\mathbf{r}, \omega) = \sum_{n=1}^N C_n(\omega) \pi_n(\mathbf{r}, \omega) \quad (5a)$$

where

$$\langle \pi_n, \hat{O} \rangle_{H_{\mathcal{V}}} = D_n(\omega) = \sum_{n'=1}^N \langle \pi_n, \pi_{n'} \rangle_{H_{\mathcal{V}}} C_{n'} \quad (5b)$$

and where

$$\langle f_1, f_2 \rangle_{H_{\mathcal{V}}} = \int_{\mathcal{V}} d^3r f_1^*(\mathbf{r}) f_2(\mathbf{r}) \quad (6)$$

is the standard inner product in H_V . Eq.(5b) can be expressed in the matrix form

$$\Pi(\omega)C(\omega) = D(\omega) \quad (7)$$

where $\Pi(\omega) = \langle \pi_n, \pi_{n'} \rangle_{H_V}$ is the $N \times N$ inner product matrix of the spanning functions π_n and $C(\omega) = [C_1(\omega), C_2(\omega), \dots, C_N(\omega)]^T$ is the column vector formed from the expansion coefficients of the pseudo-inverse Eq.(5a).

The final step of the inversion consists of diagonalizing the inner product matrix $\Pi(\omega)$ and generating a least squares inversion of Eq.(7); viz.,

$$\Pi = U\Lambda U^\dagger \Rightarrow \hat{C} = U\Lambda^+ U^\dagger D, \quad (8)$$

where Λ^+ denotes the diagonal matrix whose non-zero diagonal elements are the reciprocals of the non-zero eigenvalues $\lambda_n > 0$ of the Π matrix. As discussed in [1] the expansion Eq.(5a) with expansion coefficients determined from Eq.(8) is a least squares, pseudo-inverse of the inverse scattering problem within the DWBA. That \hat{O} is a pseudo-inverse (minimum L^2 norm solution) follows from the fact that the subspace H_Π is the pre image space (orthogonal complement of the null space) of the DWBA mapping \mathcal{P} . The fact that it is a least squares solution follows from the use of a least squares solution to the matrix equation defining the expansion coefficients.

3 Generalizations and Extensions

The inversion scheme developed in [1] and summarized above admits a number of generalizations and extensions as reported in [3]. Here we will only discuss the extension to non-point transmitter and receiver elements and to the multiple frequency case for dispersionless scattering potentials.

The basic scheme is easily generalized to be applicable to experiments employing extended planar (non-point) transmitter and receiver elements upon simple replacement of the background Green functions $G_0(\beta_j, \mathbf{r}, \omega)$ and $G_0(\mathbf{r}, \alpha_k, \omega)$ by the wave fields

$$\mathcal{G}_0(\beta_j, \mathbf{r}, \omega) = \int d^2 r' \mathcal{R}_r(\beta_j, \mathbf{r}', \omega) G_0(\mathbf{r}', \mathbf{r}, \omega), \quad (9a)$$

$$\mathcal{G}_0(\mathbf{r}, \alpha_k, \omega) = \int d^2 r' \mathcal{R}_t(\mathbf{r}', \alpha_k, \omega) G_0(\mathbf{r}, \mathbf{r}', \omega). \quad (9b)$$

The wave field $\mathcal{G}_0(\beta_j, \mathbf{r}, \omega)$ corresponds to the measured response at an extended planar sensor element located at β_j and having receiving response function $\mathcal{R}_r(\beta_j, \mathbf{r}', \omega)$ while $\mathcal{G}_0(\mathbf{r}, \alpha_k, \omega)$ is the wave field generated by an extended planar source located at α_k and having transmission response function $\mathcal{R}_t(\mathbf{r}', \alpha_k, \omega)$. For this more general situation the multistatic data matrix as defined in Eq.(1) has to be replaced by

$$\begin{aligned} \mathcal{K}_{j,k}(\omega) &= \int d^2 r'' \int d^2 r' \mathcal{R}_r(\beta_j, \mathbf{r}'', \omega) K_{\mathbf{r}'', \mathbf{r}'}(\omega) \mathcal{R}_t(\mathbf{r}', \alpha_k, \omega) \\ &= \int_V d^3 r \mathcal{G}_0(\beta_j, \mathbf{r}, \omega) O(\mathbf{r}, \omega) \mathcal{G}_0(\mathbf{r}, \alpha_k, \omega) \end{aligned}$$

where

$$K_{\mathbf{r}'', \mathbf{r}'}(\omega) = \int_V d^3 r G_0(\mathbf{r}'', \mathbf{r}, \omega) O(\mathbf{r}, \omega) G_0(\mathbf{r}, \mathbf{r}', \omega),$$

is the multistatic data matrix evaluated between the source point \mathbf{r}' and receiver point \mathbf{r}'' . With the replacement of $K_{j,k}$ with $\mathcal{K}_{j,k}$ and the spanning functions π_n by

$$\mu_n(\mathbf{r}, \omega) = \begin{cases} \mathcal{G}_0^*(\beta_j, \mathbf{r}, \omega) \mathcal{G}_0(\mathbf{r}, \alpha_k, \omega) & \text{if } \mathbf{r} \in V \\ 0 & \text{else-wise.} \end{cases}$$

the entire theory is applicable to experiments employing non-point transmitter and receiver elements characterized by the transmission and receiver response functions \mathcal{R}_t and \mathcal{R}_r .

4 Multi-frequency case for frequency independent potentials

In the theory developed in [1] and outlined above the object scattering potential is assumed to be dependent (in an unknown way) on the temporal frequency ω so that Eq.(3) is a mapping from the Hilbert space H_V of compactly supported scattering potentials at fixed frequency ω to the N -dimensional vector space $C^N(\omega)$ of complex N -tuples $D(\omega) = \{D_n(\omega)\}$ at that specific fixed frequency. In the special case where the object scattering potential is independent of ω then the basic structure of this mapping changes and becomes a mapping from the Hilbert space H_V of frequency independent scattering potentials $O(\mathbf{r})$ compactly supported in V to the tensor product of the N -tuple spaces $C^N(\omega)$ over the band of frequencies used in the set of experiments.

We can restructure the basic DWBA mapping within this new formulation as follows. First, let's assume that we have experimental data $K_{j,k}(\omega)$ at discrete frequencies $\omega = \omega_f$, $f = 1, 2, \dots, N_\omega$. In the spirit of our definition Eq.(2) we define

$$D_n = K_{j,k}(\omega_f), \quad n = j + (k-1)N_\beta + (f-1)N_\omega, \quad (10)$$

where, as before, $j = 1, 2, \dots, N_\beta$, $k = 1, 2, \dots, N_\alpha$. Eq.(10) defines an N -tuple with N now equal to $N = N_\beta \times N_\alpha \times N_\omega$ and the DWBA mapping for frequency independent scattering potentials becomes

$$\mathcal{P}O = D \quad (11)$$

where \mathcal{P} is the integral operator

$$\mathcal{P} = \int_V d^3r \pi_n^*(\mathbf{r}), \quad (12a)$$

with $\pi_n(\mathbf{r})$ defined as

$$\pi_n(\mathbf{r}) = \begin{cases} G_0^*(\beta_j, \mathbf{r}, \omega_f) G_0^*(\alpha_k, \mathbf{r}, \omega_f) & \text{if } \mathbf{r} \in V \\ 0 & \text{else-wise.} \end{cases} \quad (12b)$$

With the above definitions the pseudo-inverse employed for frequency dependent potentials can be applied with minor modification. Thus, in particular, we have as before

$$\hat{O}(\mathbf{r}) = \sum_{n=1}^N C_n \pi_n(\mathbf{r}) \quad (13a)$$

where the expansion coefficients C_n are solutions to the coupled set

$$D_n = \sum_{n'=1}^N C_{n'} < \pi_n, \pi_{n'} >_{H_V} . \quad (13b)$$

Eq. 13b can be re-written in matrix form as

$$D = \Pi C \quad (13c)$$

where $\Pi(n, n') = < \pi_n, \pi_{n'} >_{H_V}$ is the $N \times N$ inner product matrix. The least squares pseudo-inverse solution for the scattering potential is then given by Eq.(13a) with the expansion coefficients given by the least squares solution of Eq.(13c).

It is clear from the above that from a strictly computational viewpoint the inversion of frequency independent scattering potentials is structurally and formally identical to that of frequency dependent potentials. The effect of adding scattering data acquired at different frequencies is treated in the same way as would be the addition of scattering data acquired at additional transmitter or receiver points. Both of these result in an increase in the number of expansion functions $\{\pi_n\}$ generating the subspace $H_\Pi = \text{Span}\{\pi_n\}$ of H_V and, presumably, increase the dimension of this subspace and the quality of the inversion. Although transmitter and receiver location diversity and frequency diversity are formally equivalent for non-dispersive scattering potentials, they are not equivalent in terms of information content. In particular, frequency diversity is generally of more importance in reflection type experiments such as are used in pulse-echo ultrasonics, GPR (ground penetrating radar) and seismic exploration while source and receiver diversity are critical in transmission type experiments employed in tomographic type experiments [8].

5 Reformulation

The computer implementation of the single or multiple frequency inversion algorithms involves the following steps:

1. Computation of the inner product matrix

$$\Pi(n, n') = \int_{\mathcal{V}} d^3r \pi_n^*(\mathbf{r}) \pi_{n'}(\mathbf{r})$$

where $n, n' = 1, 2, \dots, N$ with $N = N_\beta \times N_\alpha \times N_\omega$,

2. Diagonalization of the inner product matrix: $\Pi = U \Lambda U^\dagger$,
3. Computation of the least square, pseudo-inverse \hat{C} of the expansion coefficient column vector C : $\hat{C} = U \Lambda^+ U^\dagger D$,
4. Computation of the least squares pseudo-inverse $\hat{O}(\mathbf{r})$:

$$\hat{O}(\mathbf{r}) = \sum_{n=1}^N \hat{C}_n \pi_n(\mathbf{r}).$$

Steps 1 and 2 are data independent and, hence, can be performed prior to actual data acquisition and, thus, do not affect the execution time of the inversion algorithm. Steps 3 and 4, on the other-hand, are performed after or in conjunction with data acquisition and can impose rather severe demands both in terms of execution time and computer storage requirements. Step 4, in particular, requires the storage of the set of spanning functions $\pi_n(\mathbf{r})$, $n = 1, 2, \dots, N$ and $\forall \mathbf{r} \in \mathcal{V}$ which can require a great deal of storage space for three-dimensional (3D) problems and/or in the multi-frequency case where the number $N = N_\beta \times N_\alpha \times N_\omega$ can be quite large even for moderately large numbers of transmitter and receiving elements. These high computational costs stem from the fact that the set of spanning functions $\{\pi_n\}$ are neither orthogonal or linearly independent with the result that the inversion is not economical in terms of computer storage or CPU time. This problem can be overcome by generating a linearly independent set either by means of the Gram-Schmidt procedure or by application of the Singular Value Decomposition (SVD) to the basic DWBA mapping Eq.(11). The SVD approach is particularly appropriate and will be employed here since it allows us to order the singular functions in order of importance according to the size of their associated singular value. Here, we will employ the SVD and derive a new formulation of the pseudo-inverse that minimizes the computational burden while retaining the same quality of inversion as obtained by the basic formulation presented in [1] and outlined above.

5.1 SVD of the DWBA mapping

To compute the SVD of the DWBA mapping it is necessary to introduce an inner product in the data space C^N and to compute the adjoint \mathcal{P}^\dagger relative to the two inner products in the spaces $H_{\mathcal{V}}$ and C^N . As before we employ the standard inner product in $H_{\mathcal{V}}$ and will also employ a standard inner product in C^N ; i.e.,

$$\langle f_1, f_2 \rangle_{H_{\mathcal{V}}} = \int_{\mathcal{V}} d^3r f_1^*(\mathbf{r}) f_2(\mathbf{r}), \quad \forall f_1, f_2 \in H_{\mathcal{V}}, \quad (14a)$$

$$\langle u_1, u_2 \rangle_{C^N} = \sum_{n=1}^N u_1^*(n) u_2(n), \quad \forall u_1, u_2 \in C^N. \quad (14b)$$

With these inner products we find that

$$\begin{aligned} \langle u, \mathcal{P}f \rangle_{C^N} &= \sum_{n=1}^N u^*(n) \int_{\mathcal{V}} d^3r \pi_n^*(\mathbf{r}) f(\mathbf{r}) \\ &= \int_{\mathcal{V}} d^3r \left\{ \sum_{n=1}^N u(n) \pi_n(\mathbf{r}) \right\}^* f(\mathbf{r}) = \langle \mathcal{P}^\dagger u, f \rangle_{H_{\mathcal{V}}} \end{aligned}$$

from which we conclude that

$$\mathcal{P}^\dagger u = \sum_{n=1}^N u(n) \pi_n(\mathbf{r}), \quad \forall u \in C^N. \quad (15)$$

The SVD of the DWBA mapping employs the singular system $\{u_p \in C^N, v_p \in H_V, \sigma_p \geq 0\}$, $p = 1, 2, \dots, N$ where

$$\mathcal{P} v_p = \sigma_p u_p, \quad \mathcal{P}^\dagger u_p = \sigma_p v_p. \quad (16a)$$

Using the singular system we then find that

$$\mathcal{P} = \sum_{p=1}^N \sigma_p u_p v_p^\dagger, \quad (16b)$$

where $v_p^\dagger : H_V \rightarrow C$ is defined in the usual way via the equation

$$v_p^\dagger f = \int_V d^3r v_p^*(\mathbf{r}) f(\mathbf{r}) = \langle v_p, f \rangle_{H_V}, \quad \forall f \in H_V,$$

and for each $p = 1, 2, \dots, N$. The singular vectors v_p and u_p are found as solution to the normal equations

$$\mathcal{P}^\dagger \mathcal{P} v_p = \sigma_p^2 v_p, \quad \mathcal{P} \mathcal{P}^\dagger u_p = \sigma_p^2 u_p. \quad (16c)$$

The functions $\{v_p(\mathbf{r}), \sigma_p \geq 0\}$ (with appropriate normalization) form an orthonormal basis in the Hilbert space H_V while the N-tuples (column vectors) $\{u_p, \sigma_p \geq 0\}$ form an orthonormal basis in C^N . Moreover, the set $\{v_p, \sigma_p > 0\}$ provides an orthonormal basis in $H_\Pi \subset H_V$ and the set $\{u_p, \sigma_p > 0\}$ provides an orthonormal basis in the image of H_Π under \mathcal{P} . *The set $\{v_p, \sigma_p > 0\}$ are, thus, precisely the set of orthonormal basis functions needed to replace the set of spanning function $\{\pi_n, n = 1, 2, \dots, N\}$ now employed in the pseudo-inverse solution developed in [1] and outlined above.*

5.2 Computing the Singular Vectors

We can write the l.h.s. of the normal equation for the singular vectors u_p in Eq.(16c) in the form

$$\begin{aligned} \mathcal{P} \mathcal{P}^\dagger u_p &= \int_V d^3r \pi_n^*(\mathbf{r}) \sum_{n'=1}^N u_p(n') \pi_{n'}(\mathbf{r}) \\ &= \sum_{n'=1}^N \left\{ \int_V d^3r' \pi_n^*(\mathbf{r}') \pi_{n'}(\mathbf{r}') \right\} u_p(n) = \Pi u_p \end{aligned}$$

where $u_p(n)$ is the n th component of the u_p singular vector and $\Pi = \langle \pi_n, \pi_{n'} \rangle_{H_V}$ is the $N \times N$ inner product matrix of the spanning functions π_n . We thus see that the normal equation for u_p is simply the matrix equation

$$\Pi u_p = \sigma_p^2 u_p \quad (17)$$

which is the diagonalizing equation for the Π matrix. In other words *the singular vectors u_p are the eigenvectors of the Π matrix and the square of the singular values σ_p^2 are the eigenvalues.*

Once the singular vectors u_p are computed the associated singular vectors v_p having non-zero singular values $\sigma_p > 0$ are computed using Eq.(16a); i.e.,

$$\sigma_p v_p = \mathcal{P}^\dagger u_p \Rightarrow v_p = \sum_{n=1}^N \frac{u_p(n)}{\sigma_p} \pi_n(\mathbf{r}), \quad (18)$$

where we have used the definition of the adjoint operator \mathcal{P}^\dagger given in Eq.(15). It is important to note that the singular vectors $u_p, v_p, \sigma_p > 0$ are data independent and can be computed prior to data acquisition and, hence, their computation will not affect the execution time or storage requirements of the reformulated inversion algorithm.

5.3 Generating the Inversion

As discussed previously, the main advantage of the new formulation is that the set $\{v_p\}$, $\sigma_p > 0$ are orthonormal and, hence, form a minimal set of functions into which the pseudo-inverse \hat{O} of the scattering potential can be expanded. Thus, in particular, it is only necessary to store the singular vectors $v_p(\mathbf{r})$ for $\sigma_p > 0$ rather than the entire spanning set $\pi_n(\mathbf{r})$, $n = 1, 2, \dots, N$. Moreover, as we will show below, only projections $\langle v_p, O \rangle_{H_V}$ of the scattering potential associated with singular vectors whose singular values σ_p exceed some threshold value $\sigma_p > \epsilon > 0$ can be reliably computed in the presence of additive noise or measurement error so that only those singular vectors whose singular values satisfy this condition need be retained and used in the inversion. The threshold value ϵ is a regularization parameter that can be selected to balance noise tolerance versus accuracy of the inversion algorithm. We mention that the new formulation still requires that the Π matrix be computed and then diagonalized as in the old scheme. After that the eigenvectors and eigenvalues of Π are used to compute the singular vectors v_p using Eq.(18). The inversion can then be generated directly from the stored singular system $\{v_p, u_p, \sigma_p > \epsilon\}$ as we will now describe.

To compute the pseudo-inverse we first represent the data vector D in the basis u_p ; i.e.,

$$D = \sum_{p=1}^N \langle u_p, D \rangle_{C^N} u_p. \quad (19a)$$

In a similar manner we can expand the unknown object profile O into the set of singular vectors v_p :

$$O = \sum_{p=1}^N \langle v_p, O \rangle_{H_V} v_p. \quad (19b)$$

If we now substitute this set of equations into the DWBA mapping $PO = D$ we find that

$$\sum_{p=1}^N \sigma_p \langle v_p, O \rangle_{H_V} u_p = \sum_{p=1}^N \langle u_p, D \rangle_{C^N} u_p \quad (20a)$$

from which we conclude that

$$\langle v_p, O \rangle_{H_V} = \frac{\langle u_p, D \rangle_{C^N}}{\sigma_p}, \quad (20b)$$

if $\sigma_p > 0$. The pseudo-inverse is thus given by

$$\hat{O} = \sum_{\sigma_p > 0} \frac{\langle u_p, D \rangle_{C^N}}{\sigma_p} v_p. \quad (20c)$$

As I remarked above, in the case where additive noise is present we would like to regularize the expansion Eq.(20c) by setting a threshold $\epsilon > 0$ and using only singular values and associated singular vectors for which $\sigma_p > \epsilon$. The sensitivity of the inversion \hat{O} to additive noise or other errors in the data vector is apparent from Eq.(20c) which shows that small changes in $\langle u_p, D \rangle_{C^N}$ are magnified by the presence of σ_p in the denominator of the expression for \hat{O} . Such a regularization, which is data independent, not only increases the robustness of the reconstruction but it also decreases the number of singular functions that need to be stored so that both computer storage requirements as well as CPU execution time are decreased. We will examine the regularization issue for a number of test cases in section 6.

6 Computer Simulation

The inverse scattering algorithms developed in the grant and outlined above were tested in computer simulations in both [1] and [3]. Here we will only present the simulations given in [3] since they encompass the results presented in the earlier paper and are generated from the optimal form of the reconstruction algorithm. In the simulations we employed a simple non-dispersive background model consisting of a uniform, constant velocity medium with and without a perfectly reflecting bottom layer in which is embedded a small

non-dispersive scattering potential. The scatterer is assumed to be embedded in a rectangular grid with x denoting horizontal position and z vertical position with positive z directed downward. In cases where we employ a set of frequencies ω_f , $f = 1, 2, \dots, N_\omega$ we define a center frequency ω_c which results in a center wavelength $\lambda_c = 1$ from which we will reference all of our distances. In particular, the grid spacing is selected to be one tenth of this wavelength ($\delta x = \delta z = 1/10$). In all simulations the transmitter array was located on the top row of the rectangular grid and the receiver array along the left hand side of this grid. When present, the reflecting bottom was placed along the bottom row of the grid.

The object of the simulations is first to examine the performance of the algorithm for frequency independent scattering potentials when multiple distinct frequencies are used as discussed in section 4 and to compare the reconstructions obtained in this case with results obtained using only a single frequency. A second goal is to determine the computer storage gain obtained when using the SVD based inversion algorithm of section 5. In all the simulations we assume point source excitation and point receivers and do not test the effect of extended sources or receivers on the performance of the inversion algorithm. Also, as was the case in [1], the simulations test the performance of the inversion algorithm and *not* the validity of the DWBA which is outside the scope of this paper. We therefore computed the scattered field data (multistatic data matrix) within the DWBA according to Eq.(1) using the above mentioned background consisting of either a uniform constant velocity background or a uniform background with a bottom reflecting layer.

6.1 Test Cases

The simulations were performed on a $5\lambda_c \times 6\lambda_c$ image grid ($= \mathcal{V}$) with one-tenth center wavelength sampling as discussed above. The sources were located on the top row of the support grid with cases of $N_\alpha = [3, 5, 7, 9]$ elements while the receivers were located on the left hand side of the grid also with cases $N_\beta = [3, 5, 7, 9]$. The simulations were also performed at a number of frequencies $\omega = [2\omega_c, \omega_c, \frac{2}{3}\omega_c, \frac{1}{2}\omega_c]$ which result in wavelengths of $\lambda = [\frac{1}{2}\lambda_c, \lambda_c, \frac{3}{2}\lambda_c, 2\lambda_c]$ with λ_c set to a value of unity.

We used two objects with different characteristics. First was a composite object consisting of a set of 5 real valued circular discs having diameter $\lambda_c/2$ distributed at the corners and center of a square $3\lambda_c$ per side. We will call this **Object 1**. The second object is a rectangle centered in \mathcal{V} with dimensions $3\lambda_c \times 2\lambda_c$. Embedded in this square is another rectangle of dimensions $1\lambda_c \times \lambda_c/2$. We will call this **Object 2**. Tests for both objects were performed both with and without the reflecting bottom and also with and without additive white Gaussian measurement noise (AWGN) although we only present the results for the cases that provide information we did not see in [1].

As was the case in [1] the Green functions needed to compute the spanning functions $\{\pi_n(\mathbf{r}), n = 1, 2, \dots, N\}$ are constructed from a Hankel function of the first kind whose argument is a function only of the distance between the field point (or its mirror image about the reflecting bottom) and the source or receiver location. In the case of a uniform background model the spanning functions are found to be given by

$$\pi_n(\mathbf{r}, \omega_f) = \begin{cases} G_0^*(\beta_j - \mathbf{r}, \omega_f) G_0^*(\alpha_k - \mathbf{r}, \omega_f) & \text{if } \mathbf{r} \in \mathcal{V} \\ 0 & \text{else-wise} \end{cases} \quad (21)$$

where

$$G_0(\mathbf{R}, \omega_f) = -\frac{i}{2} H_0(k_{\omega_f} |\mathbf{R}|)$$

where H_0 is the zero order Hankel function of the first kind and k_{ω_f} is the background wavenumber for the given frequency ω_f . In the case of a perfect reflecting bottom the background Green function is given by

$$G_b(\mathbf{r}, \mathbf{r}', \omega_f) = G_0(|\mathbf{r} - \mathbf{r}'|, \omega_f) - G_0(|\mathbf{r} - \tilde{\mathbf{r}}'|, \omega_f)$$

where we have used the subscript “b” to denote the reflecting bottom Green function and where $\tilde{\mathbf{r}}'$ is the mirror image of the point \mathbf{r}' about the bottom; i.e., $\tilde{\mathbf{r}}' = (x', -z' - 2l_0)$ where l_0 is the distance of the bottom from the top of the grid. In the case of a reflecting bottom the spanning functions are thus computed using Eq.(21) with the background Green function replaced by G_b .

To analyze the performance of the algorithm in the presence of noise, we used additive white Gaussian noise (AWGN) which was added to the data vector D such that the noisy data $D_\eta = D + \mathcal{N}$ and $\mathcal{N} = \mathcal{N}(0, \sigma^2 I)$. The noise variance was taken to be 2% of the largest component of the D vector.

6.2 Multiple Frequencies

The use of multiple frequencies in the reconstruction of non-dispersive objects is illustrated in figures 1-3. In figures 1 and 2, we see the difference between the reconstructions for Object 1 and Object 2 when we use the data obtained by performing the scattering experiment with one frequency and then with four frequencies. As we would expect, the reconstruction quality improves dramatically as we add the new data. In particular, the extended square, Object 2, which is completely unresolved at a single frequency, is well resolved with four. An interesting thing to note is the improvement in the ability of the algorithm to represent the part of the object that is farther away from the array. This is critical as most practical applications will not have array coverage on all sides of the image grid and, as we saw from part I, even large arrays at a single frequency will not generate adequate data to accurately recreate the far edge of the grid. These results are consistent with other attempts at using multiple frequency data within the DWBA [13].

In section 4 we mentioned that in reflection type experiments frequency diversity is more important than source receiver diversity. The offset VSP type of experiment that we are simulating here is intermediate between a reflection and transmission type of experiment [8]; when we use the reflecting bottom, the experiment is more like a reflection experiment and without the bottom it is more like a transmission experiment. We should then expect that frequency diversity is a more important factor in the quality of the reconstruction when the reflecting bottom is used and diversity in the source/receiver positions to be more important without the bottom. To illustrate this, we performed simulations with the reflecting bottom and with comparable amounts of data, one diverse in frequency and the other diverse in receiver position. The results for the reflection type experiment are shown in figure 3 while the results of the transmission type experiment are shown in figure 4. In figure 3(a,b) we can see the reconstructions for a 7×7 array at a single frequency and for a 5×5 array at two frequencies which use 49 and 50 data points respectively. In figure 3(c,d) we used a 9×9 single frequency array and a 5×5 array at three frequencies, which use 81 and 75 data points. After comparing these reconstructions, we can see that the diverse frequency arrays outperform the single frequency arrays. The single frequency arrays do a better job of representing the disk in the upper left corner but cannot give any indication of the two discs along the bottom. In figure 4 we do the same comparison without the reflecting bottom. It is clear from this figure that the diversity in the position of sources/receivers produce a much sharper picture in this experiment which again is closely related to a transmission experiment.

6.3 SVD Inversion Scheme

To examine the performance of the SVD based formulation of the inversion scheme, we investigated the consequences of changing the level of ϵ . For noise-free data, as we set the threshold higher and higher, the number of singular values we keep decreases and therefore the quality of the reconstruction will decrease. At the same time however, the time to compute the reconstruction as well as the amount of storage needed for the singular functions decreases, which is the goal of the new formulation. In fact, the storage space and reconstruction time are both linear functions of the number of singular values with the same rate of change, so we can think of these qualities as equivalent in terms of their change. In the case of noisy data, as we set the threshold lower and lower, we will get a better reconstruction until a point when the singular values become too small and the reconstruction is dominated by noise. It is at this point that we would like to compute the reconstructions and determine how much storage space was saved.

We first performed simulations with noise-free data, varying ϵ so that in each test 10% of the singular values were dropped. Looking at figures 5 and 6, we can see the results of these tests. We see that the reconstruction is almost unchanged even when we remove 50% of the singular values. While it is obvious that the quality of the reconstruction will drop as we remove singular values, we are also interested in how this compares to the storage space needed for the singular functions. Looking at figure 7 we can see these results for our tests. Here we have plotted the percentage decrease in the time to compute the reconstruction for some $N\%$ of the singular values defined as

$$\delta T_{N\%} = \frac{T_{100\%} - T_{N\%}}{T_{100\%}}$$

where $T_{100\%}$ is the time compute the reconstruction using all singular values, against the percent reconstruc-

tion error, defined as

$$E_R = \int_V d^2r \frac{|O(\mathbf{r}) - \hat{O}(\mathbf{r})|^2}{|O(\mathbf{r})|^2} \approx \sum_n \delta x \delta z \frac{|O(\mathbf{r}_n) - \hat{O}(\mathbf{r}_n)|^2}{|O(\mathbf{r}_n)|^2}. \quad (22)$$

We see that for each of the tests, as we remove 10% of the singular values for a test, we also get a 10% reduction in the time to compute the reconstruction. What is interesting is that the percentage error is not increasing at that fast of a rate, especially in the range of 50 – 100% of singular values. This tells us that when keeping between 50 – 100% of the singular values, for a reasonably small decrease in reconstruction quality, we get a very large performance increase in terms of reconstruction time.

In the noisy cases, we need to determine the threshold at which we need to start to drop singular values to obtain a reasonable reconstruction. This would give us a clear picture of how much storage and time we could save while still producing the optimal reconstruction. In figure 8, we can see the noisy reconstructions of Object 2 for four sets of frequencies, two of which we have seen the in the noise-free cases of figure 1. We can see here that the objects were still reconstructed quite well, although we also see that there is a limit to how much data we can add for a given experiment as the addition of the fourth frequency in figure 8(d) does not add much to the reconstruction. The main purpose of these experiments was to determine how many of the singular values we are able to discard, and by looking at figure 9, we can see that we were able to eliminate 5 – 30% of the singular values, corresponding to an equivalent reduction in computation time and storage space. We can also see that the percentage kept was well within the region we defined above as having a small impact on reconstruction quality which is why we were able to get quality reconstructions while reducing the storage needs by this amount.

It is also important to mention that the thresholds that were obtained were done so with the use of the object profile which allows us to calculate an error value for each amount of singular values kept. Without knowledge of the object profile, the calculation of the threshold becomes a much harder problem and is beyond the scope of this paper. Attempts to work on this problem are detailed in [14].

7 Summary

In this grant the inverse scattering problem was formulated and solved within the distorted wave Born approximation (DWBA). The theory is general and applies to both dense and sparse transmitter and receiver arrays that are arbitrarily distributed in space and whose elements can be extended and have arbitrary radiation patterns. Inversion algorithms have been derived and tested in computer simulations that yield a pseudo-inverse of the inverse scattering problem from either single frequency or broad band scattering data. An important feature of the theory and inversion algorithms is that they incorporate a priori knowledge of both the background in which the unknown scatterers are embedded as well as estimates of the support volume of the scatterers.

Future work in this area will focus on its extension to vector valued fields (e.g., electromagnetic and elastic waves) and to the use of regularization methods other than the SVD. It is also planned to apply the algorithm to real data sets acquired in both electromagnetic as well as elastic wave scattering experiments currently being planned.

References

- [1] A.J. Devaney and M. Dennison, "Inverse Scattering In Inhomogeneous Background Media," *Inverse Problems* **19**, No. 4(August 2003), 855-870.
- [2] J.H. Taylor, *Scattering Theory* (Wiley, New York, 1972).
- [3] M. Dennison and A.J. Devaney, 'Inverse scattering in inhomogeneous background media: Part II SVD analysis and multiple frequency case, *Inverse Problems*, **20**, 1307-1324 (2004)
- [4] C. Prada and M. Fink, "Eigenmodes of the time reversal operator: A solution to selective focusing in multiple-target media", *Wave Motion* **20** 151-163 (1994).

- [5] S. Komilikis, C. Prada and M. Fink, "Characterization of extended objects with the D.O.R.T. method", *Proceedings of the IEEE Ultrasonics Symposium 1996*, Vol. 2, 1401-1404.
- [6] T.D. Mast, A.I. Nachman, and R.C. Wagg, "Focusing and imaging using eigenfunctions of the scattering operator," *J. Acoust. Soc. Am.* **102**(2) 715-725 (1997).
- [7] A.J. Devaney and M. Oristaglio, "Inversion procedure for inverse scattering within the distorted wave Born approximation," *Phys. Rev. Letts.* **51**, p. 237 (1983). (with M. Oristaglio).
- [8] A.J. Devaney, "Geophysical diffraction tomography," *IEEE Trans. Geoscience and Remote Sensing* Vol. **GE-22**, p. 3, 1984.
- [9] A.J. Devaney, "Inverse Source and Scattering Problems In Ultrasonics", *IEEE Trans. Sonics and Ultrasonics*, Vol. **SU-30**, 6, 1983.
- [10] D.H. Chambers and A. K. Gautesen, "Time reversal for a single spherical scatterer," *J. Acoust. Soc. Am.*, **109**, 2616-2624, 2001.
- [11] D.H. Chambers, "Analysis of the time-reversal operator for scatterers of finite size," *Journal of the Acoustical Society of America*, **112**, pp.411-419 (2002).
- [12] M.Fink, D. Cassereau, A.Derode, C.Prada, P. Roux, M. Tanter, J-L. Thomas and F. Wu, "Time reversed acoustics," *Rep. Prog. Phys.*, **63**, pp.1933-1995 (2000).
- [13] A. G. Tijhuis et al, "Multiple-frequency distorted-wave Born approach to inverse profiling", *Inverse problems*, **17**, 1635-1644 (2001).
- [14] C. Vogel, *Computational Methods for Inverse Problems* Siam, Philadelphia, 2002.

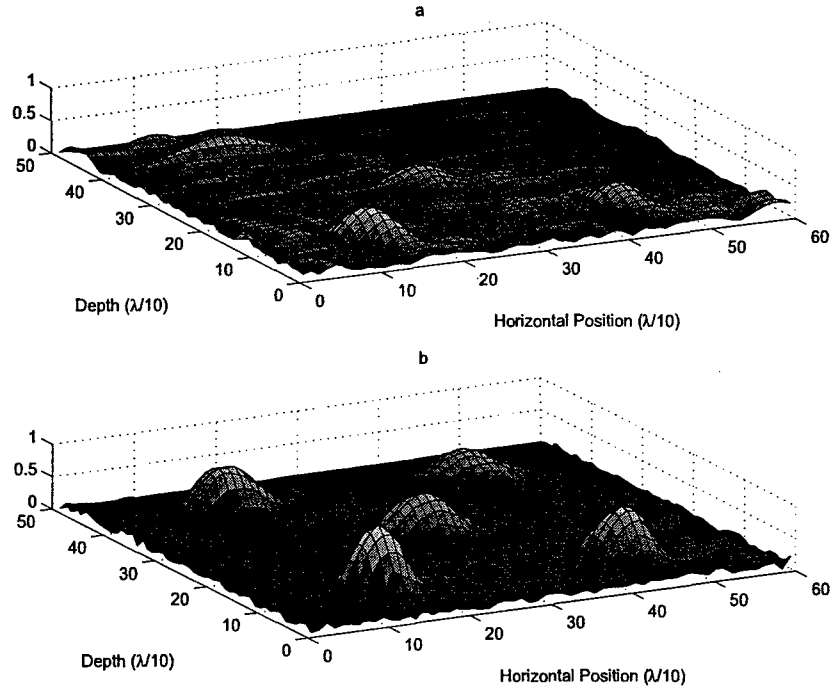


Figure 1: Reconstructions of Object 1 for multiple frequencies with reflecting bottom. Shown are surface plots of the absolute value of the reconstructions for (a) $\lambda = [\lambda_c]$ (b) $\lambda = [\frac{1}{2}\lambda_c, \lambda_c, \frac{3}{2}\lambda_c, 2\lambda_c]$. Both reconstructions performed for $N_\alpha = N_\beta = 9$.

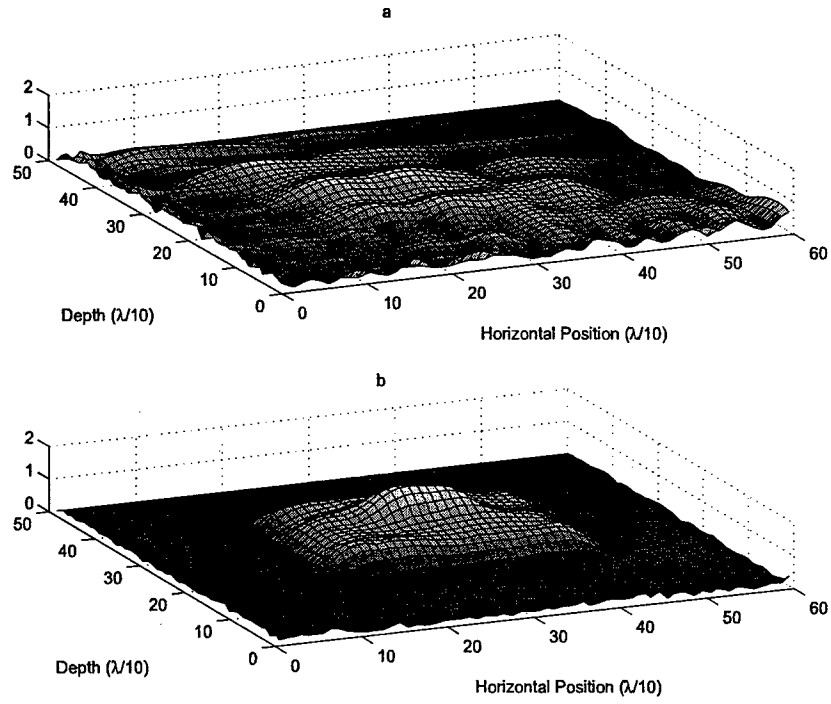


Figure 2: Reconstructions of Object 2 for multiple frequencies with reflecting bottom. Shown are surface plots of the absolute value of the reconstructions for (a) $\lambda = [\lambda_c]$ (b) $\lambda = [\frac{1}{2}\lambda_c, \lambda_c, \frac{3}{2}\lambda_c, 2\lambda_c]$. Both reconstructions performed for $N_\alpha = N_\beta = 9$.

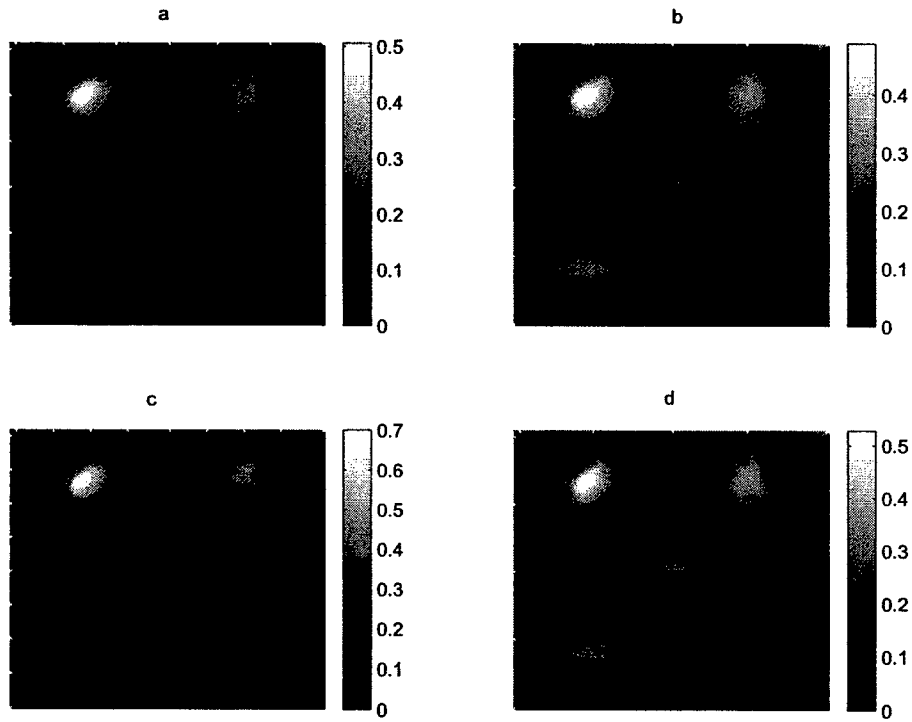


Figure 3: Reconstructions of Object 1 comparing single and multiple frequencies **with** reflecting bottom. Shown are the reconstructions for (a) $N_\alpha = N_\beta = 7$ and $\lambda = [\lambda_c]$ (b) $N_\alpha = N_\beta = 5$ and $\lambda = [\lambda_c, \frac{3}{2}\lambda_c]$ (c) $N_\alpha = N_\beta = 9$ and $\lambda = [\lambda_c]$ (d) $N_\alpha = N_\beta = 5$ and $\lambda = [\frac{1}{2}\lambda_c, \lambda_c, \frac{3}{2}\lambda_c]$.

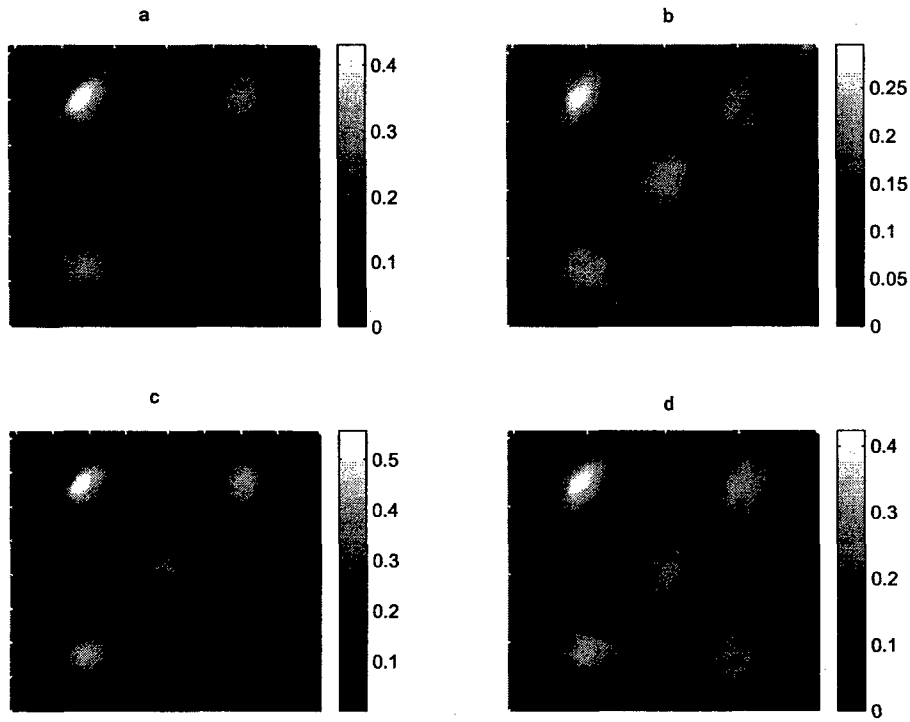


Figure 4: Reconstructions of Object 1 comparing single and multiple frequencies with **no** reflecting bottom. Shown are the reconstructions for (a) $N_\alpha = N_\beta = 7$ and $\lambda = [\lambda_c]$ (b) $N_\alpha = N_\beta = 5$ and $\lambda = [\lambda_c, \frac{3}{2}\lambda_c]$ (c) $N_\alpha = N_\beta = 9$ and $\lambda = [\lambda_c]$ (d) $N_\alpha = N_\beta = 5$ and $\lambda = [\frac{1}{2}\lambda_c, \lambda_c, \frac{3}{2}\lambda_c]$.

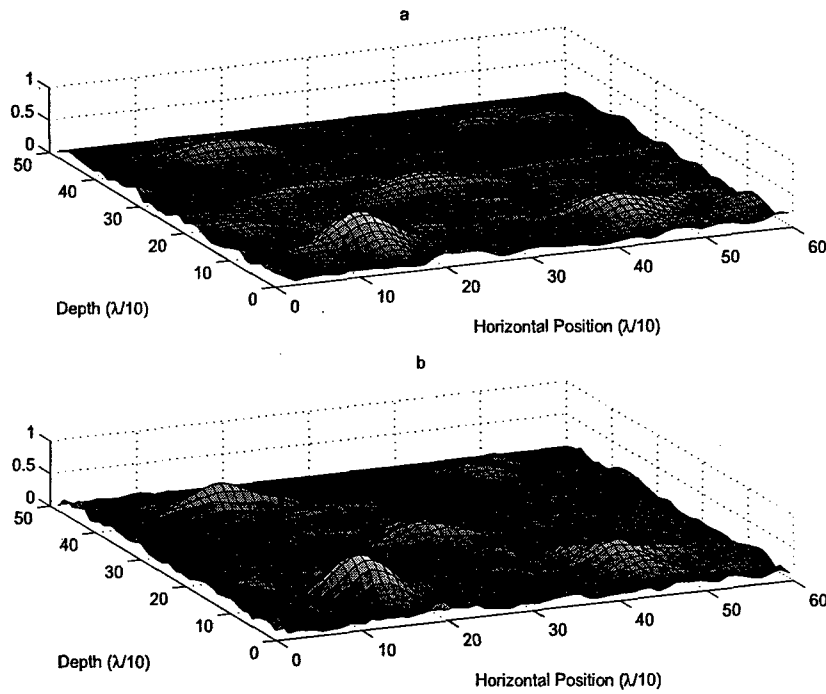


Figure 5: Surface plots of the reconstruction of Object 1 for (a) 50% and (b) 100% of singular values kept and noise free data. Reconstructions performed with $N_\alpha = N_\beta = 7$ and $\lambda = [\frac{1}{2}\lambda_c, \lambda_c, \frac{3}{2}\lambda_c]$.

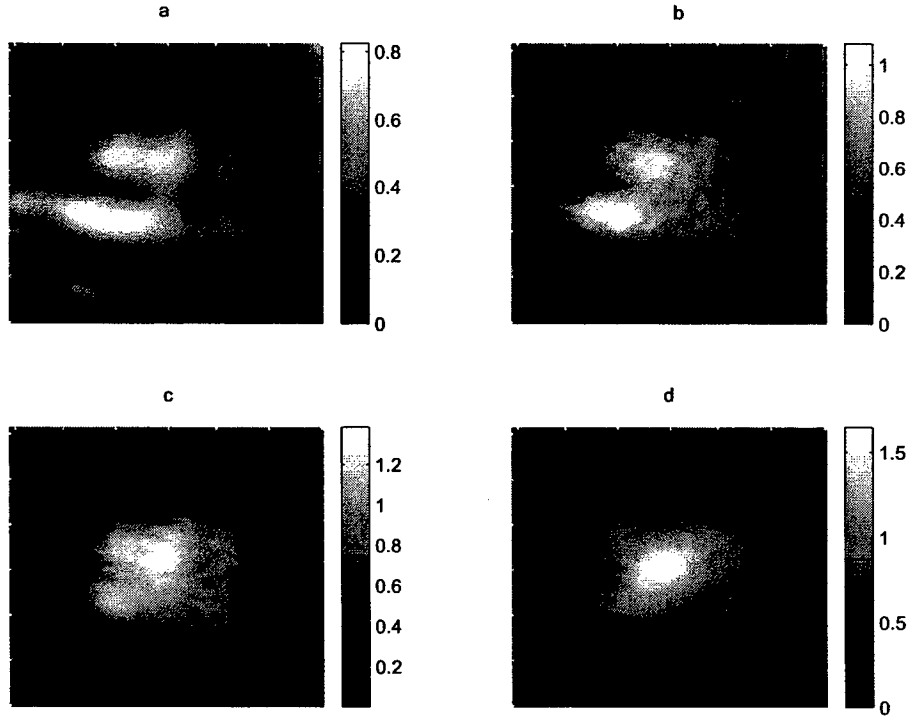


Figure 6: Reconstructions of Object 2 for varying number of singular values kept and noise free data. Shown are the reconstructions for (a) 25% (b) 50% (c) 75% (d) 100%. All reconstructions performed for $N_\alpha = N_\beta = 7$ and $\lambda = [\frac{1}{2}\lambda_c, \lambda_c, \frac{3}{2}\lambda_c]$.

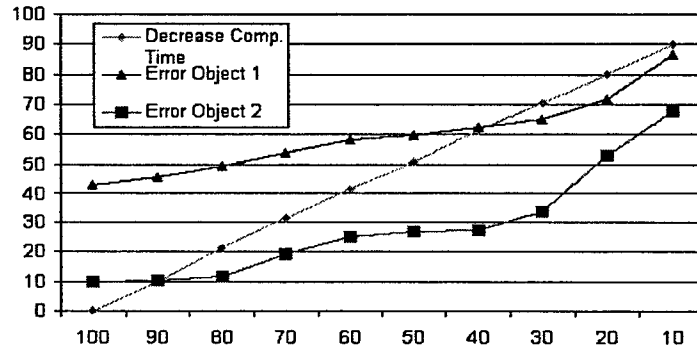


Figure 7: Graph of percentage time gained ($\delta T_{N\%}$) and percentage reconstruction error (E_R) for varying numbers of singular values kept. All data was obtained for reconstructions using $N_\alpha = N_\beta = 7$ and $\lambda = [\frac{1}{2}\lambda_c, \lambda_c, \frac{3}{2}\lambda_c]$.

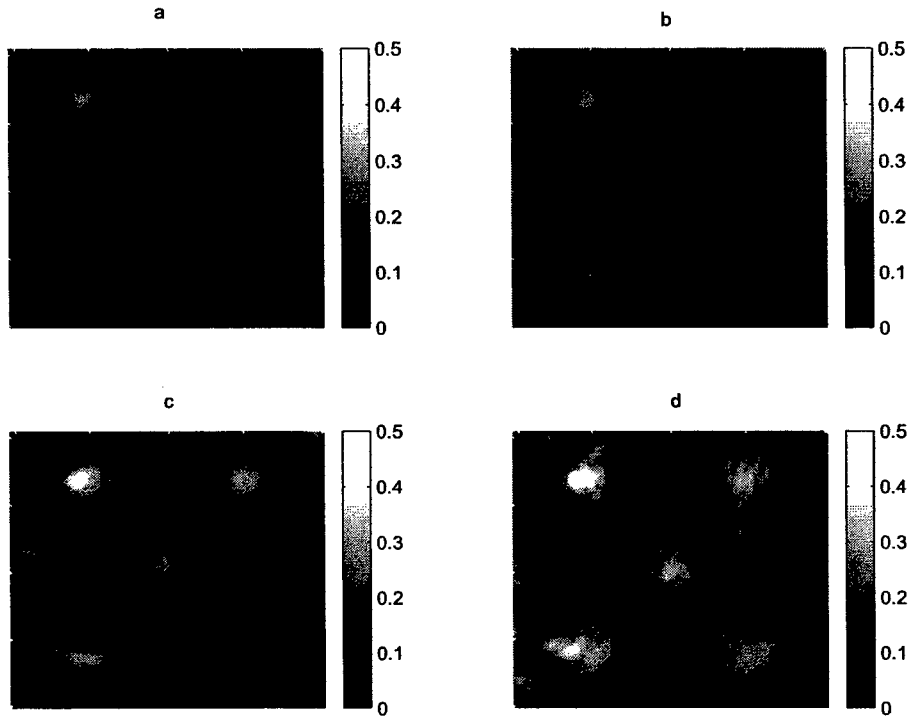


Figure 8: Reconstructions of Object 1 for multiple frequencies with noisy data and reflecting bottom. Shown are the reconstructions for (a) $\lambda = [\lambda_c]$ (b) $\lambda = [\lambda_c, \frac{3}{2}\lambda_c]$ (c) $\lambda = [\frac{1}{2}\lambda_c, \lambda_c, \frac{3}{2}\lambda_c]$ (d) $\lambda = [\frac{1}{2}\lambda_c, \lambda_c, \frac{3}{2}\lambda_c, 2\lambda_c]$. All reconstructions performed for $N_\alpha = N_\beta = 5$.

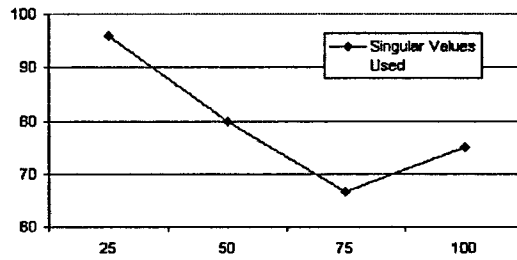


Figure 9: Graph of the percentage of singular values kept for the reconstructions of Object 2 as seen in Fig. 8 plotted against the number of total singular values.